PHYSICAL REVIEW B **105**, 104431 (2022)

Breakdown of atomic spin-orbit coupling picture in an apparently isolated pseudo-one-dimensional iridate: Sr_3NaIrO_6

Abhisek Bandyopadhyay,[1,2] A. Chakraborty,[3] S. Bhowal,[3,4] Vinod Kumar,[5] M. M. Sala,[6,7] A. Efimenko,[6] F. Bert,[8] P. K. Biswas,[9] C. Meneghini,[10] N. Büttgen,[11] I. Dasgupta,[3] T. Saha Dasgupta,[12] A. V. Mahajan,[5] and Sugata Ray[1,*]

[1]*School of Materials Sciences, Indian Association for the Cultivation of Science,*
2A & 2B Raja S. C. Mullick Road, Jadavpur, Kolkata 700 032, India
[2]*Department of Physics, Indian Institute of Science Education and Research, Pune, Maharashtra 411008, India*
[3]*School of Physical Sciences, Indian Association for the Cultivation of Science,*
2A & 2B Raja S. C. Mullick Road, Jadavpur, Kolkata 700 032, India
[4]*Materials Theory, ETH Zurich, Wolfgang-Pauli-Strasse 27, 8093 Zurich, Switzerland*
[5]*Department of Physics, Indian Institute of Technology Bombay, Powai, Mumbai 400076, India*
[6]*ESRF–The European Synchrotron, 71 Avenue des Martyrs, 38000 Grenoble, France*
[7]*Dipartimento di Fisica, Politecnico di Milano, Piazza Leonardo da Vinci 32, 20133 Milano, Italy*
[8]*Université Paris-Saclay, CNRS, Laboratoire de Physique des Solides, 91405 Orsay, France*
[9]*ISIS Facility, Rutherford Appleton Laboratory, Chilton, Didcot, Oxon OX110QX, United Kingdom*
[10]*Dipartimento di Scienze, Universitá Roma Tre, Via della Vasca Navale 84, 00146 Rome, Italy*
[11]*Experimental Physics V, Center for Electronic Correlations and Magnetism, University of Augsburg, 86159 Augsburg, Germany*
[12]*Department of Condensed Matter Physics and Material Sciences, S. N. Bose National Centre for Basic Sciences,*
Block JD, Sector 3, Saltlake, Kolkata 700106, India

(Received 6 July 2021; revised 11 March 2022; accepted 11 March 2022; published 28 March 2022)

In the presence of strong atomic spin-orbit coupling (SOC), tending to the j-j coupling limit, $5d^4$ iridates are speculated to possess a nonmagnetic $J_{\rm eff} = 0$ singlet ground state from atomic consideration, which invariably gets masked due to different solid-state effects (e.g., hopping). Here, we try to probe the trueness of the atomic SOC-based proposal in an apparently one-dimensional system, Sr_3NaIrO_6, with well-separated Ir^{5+} ($5d^4$) ions. But all the detailed experimental as well as theoretical characterizations reveal that the ground state of Sr_3NaIrO_6 is not nonmagnetic. However, our combined dc susceptibility χ, ^{23}Na nuclear magnetic resonance (NMR), muon spin relaxation/rotation (μSR), and heat capacity C_p measurements clearly refute any sign of spin freezing or ordered magnetism among the Ir^{5+} moments due to geometrical exchange frustration, while in-depth zero-field and longitudinal field μSR investigations strongly point towards an inhomogeneous quantum spin liquid (QSL)-like ground state. In addition, the linear temperature dependence of both the NMR spin-lattice relaxation rate and the magnetic heat capacity at low temperatures suggest low-lying gapless spin excitations in the QSL phase of this material. Finally, we conclude that the effective SOC realized in d^4 iridates is unlikely to offer a ground state which will be consistent with a purely atomic j-j coupling description.

DOI: 10.1103/PhysRevB.105.104431

I. INTRODUCTION

Heavier $4d$ and $5d$ transition metal oxides possess strong spin-orbit coupling (SOC) and crystal field splitting energy Δ with moderate Coulomb repulsion U and have been at the center of condensed-matter physics research for more than a decade now. The reason for this is the growing excitement surrounding the realization of exotic electronic and magnetic ground states in such systems within these parameter ranges [1,2]. However, from a technology perspective, one big challenge has been to untie the complex, interconnected knot of several electronic parameters as every attempt to independently manipulate one crucial parameter has invariably modulated others, often in a direction adverse to the desired result. Therefore, the search for a suitable material playground remains ongoing.

Here, another attempt is made to realize the coveted $J_{\rm eff} = 0$ nonmagnetic ground state, derived from the purely atomic j-j coupling description of Ir^{5+} ($5d^4$) in a new candidate, Sr_3NaIrO_6 (SNIO), with quasi-one-dimensional (quasi-1D) structure. The structure of the compound, obtained from the Rietveld refinement of the room temperature x-ray diffraction (XRD) pattern (Fig. S1 of the Supplemental Material (SM) [3]), consistent with a previous study [4], is shown in Fig. 1(a). This compound possesses a 1D-like structure in which alternating IrO_6 octahedra and trigonal prismatic NaO_6 units form a column along the c direction. The interchain Ir-Ir distances are reasonably large (5.9 and 6.78 Å), and the Ir-O-Na-O-Ir intrachain superexchange interactions are anticipated to be rather small, resulting in a nearly isolated magnetic and electronic environment for Ir. Such a situation

---

[*] mssr@iacs.res.in

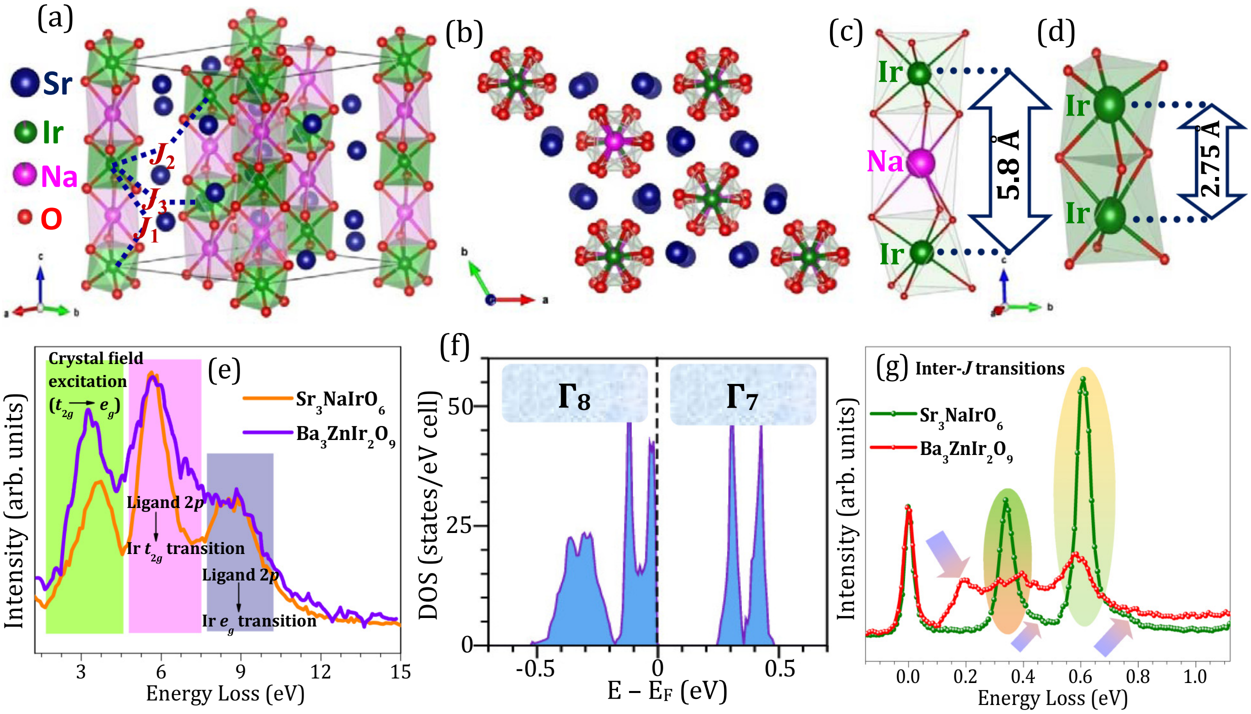

FIG. 1. (a) Crystal structure of SNIO with Ir-Ir exchange pathways (dotted blue lines). (b) Isolated 1D chains in the *ab* plane. Ir-Ir hopping pathways for (c) SNIO and (d) 6*H*-$Ba_3ZnIr_2O_9$ (BZIO). Comparison of Ir L_3 RIXS spectra in (e) low-resolution, high-energy features and (g) high-resolution, low-energy excitations. (f) The total density of states (DOS) of SNIO within GGA + SOC.

naturally points towards narrower Ir bands, reduced hopping, and, consequently, increased SOC and an enhanced possibility of realizing the $J_{\text{eff}} = 0$ state in SNIO.

But it should be noted that such 1D systems are not devoid of controversy regarding their true dimensionality [5–10]. It was shown recently [11] that the $A_2B\text{IrO}_6$ iridates have essentially zero O $2p$ to Ir $5d$ charge-transfer energies, leading to unusually strong covalent interaction and significantly large effective Ir-O-O-Ir magnetic exchange interactions. Most importantly, Liu *et al.* [12] also showed, using resonant inelastic x-ray scattering (RIXS) experiments on Sr_3CuIrO_6, that the expectation of a strong SOC limit in these systems could be deceptive.

Amid these controversies over the true dimensionality and the actual strength of SOC in columnar iridates, our results for SNIO not only indicate a breakdown of the possible $J_{\text{eff}} = 0$ state but also reveal that Ir^{5+} possesses one of the highest magnetic moments ($\sim 0.5\mu_B$) in SNIO among the $5d^4$ iridates. Our combined dc susceptibility, ^{23}Na NMR, and muon spin relaxation/rotation (μSR) studies, together with the *ab initio* density functional theory (DFT) calculations, confirm that despite having noticeable antiferromagnetic (AFM) interactions among the large local Ir^{5+} moments ($\Theta_{CW} = -23.6$ K), SNIO fails to trigger any magnetic order down to at least 40 mK due to enhanced quantum fluctuations as a result of geometrical frustration arising from the triangular network see Fig. 3(d) below, and consequently, a gapless quantum spin liquid (QSL) state is stabilized. Last, considering the presence of the finite Ir^{5+} moment in this pseudo-1D system, we go on to compare the bandwidth vs moment trends of SNIO with other d^4 iridates and conclude that only a moderate SOC, far from j-j coupling, should be applicable to all these iridates.

II. METHODOLOGY

A. Experimental techniques

The polycrystalline Sr_3NaIrO_6 sample was synthesized using the conventional solid-state reaction technique using stoichiometric amounts of high-purity (>99.9%) predried $SrCO_3$, Na_2CO_3, and IrO_2 as starting materials. These starting materials were homogeneously ground and calcined at 700 °C in air for 12 h, and finally, the resultant mixture was reground and annealed at several higher temperatures (800 °C and 900 °C for 12 h each) in air with few intermediate grindings. The phase purity of the sample was checked by x-ray powder diffraction measured with a Bruker AXS: D8 Advance x-ray diffractometer with Cu $K\alpha$ radiation at room temperature. The obtained XRD data were analyzed by using the Rietveld technique, and the structural refinement was performed using the FULLPROF program [13]. The Ir L_3-edge x-ray absorption near-edge structure (XANES) and extended x-ray absorption fine-structure (EXAFS) measurements for this sample were performed at the XAFS beamline of the Elettra (Trieste, Italy) synchrotron radiation facility at room temperature in standard transmission geometry. The data treatment and quantitative analysis of EXAFS were performed using the freely available DEMETER package [14,15] (ATHENA and ARTEMIS programs) using atomic clusters generated from crystallographic structure. To verify the chemical homogeneity and any cation off-stoichiometry in the sample, energy dispersive x-ray analysis was also performed using a field emission scanning electron microscope (JEOL, JSM-7500F). The cation stoichiometry was also checked by inductively coupled plasma–optical emission spectroscopy using a Perkin Elmer Optima 2100 DV instrument. The x-ray photoemission spectroscopy (XPS) measurements were carried out using an Omicron electron spectrometer, equipped with a Scienta Omicron Sphera analyzer and an Al $K\alpha$ monochromatic source with an energy resolution of 0.5 eV. Before the experiment, sample surface cleaning was achieved by optimized sputtering with argon ion bombardment to remove any kind of surface oxidation effect and the presence of environmental carbons in the pelletized samples. The collected spectra were processed and analyzed with the KOLXPD program. Electrical resistivity was measured by the standard four-probe method within the temperature range of 150–400 K in a physical property measurement system (PPMS, Cryogenic). Magnetization measurements for this sample were carried out in the temperature range of 2–300 K and in magnetic fields up to ±50 kOe in a superconducting quantum interference device magnetometer (Quantum Design). Further, heat capacity was measured within the 2–300 K temperature range in a PPMS (Quantum Design) in the zero field as well as several applied higher magnetic fields (up to 90 kOe). The μSR experiments, as a local magnetic probe, were conducted with the EMU spectrometer at the ISIS large-scale facility in both a helium flow cryostat and a dilution fridge. Moreover, the RIXS measurements at the Ir L_3 edge of the polycrystalline Sr_3NaIrO_6 sample (in powder form) were performed at $T = 20$ and 300 K at the ID20 beamline of the European Synchrotron Radiation Facility (ESRF) using π-polarized photons and a scattering geometry with $2\theta \simeq 90^\circ$ to suppress elastic scattering. A spherical, diced Si(844) analyzer was used in a Rowland circle with a 2 m radius in combination with a custom-built hybrid pixel detector, with an overall energy resolution of ≈29 meV at the Ir L_3 edge in this configuration. During the experiment, the incident photon energy was kept fixed at 11.216 keV, which was found to enhance the low-energy inelastic features of the J multiplet excitations. Both the low-resolution, high-energy and high-resolution, low-energy Ir L_3 RIXS spectra for SNIO are for $T = 20$ K. The 20 K Ir L_3-edge RIXS spectra (both high resolution, low energy and low resolution, high energy) of the isovalent d^4 $6H$-hexagonal iridate $Ba_3ZnIr_2O_9$ (BZIO; powder form) were also collected within the same technical specifications as SNIO for comparison.

B. Theoretical details

The electronic structure calculations based on DFT presented in this paper were carried out in the plane-wave basis within the generalized gradient approximation (GGA) [16] of the Perdew-Burke-Ernzerhof exchange correlation supplemented with Hubbard U as encoded in the Vienna Ab initio Simulation Package (VASP) [17,18] with projector augmented wave potentials [19,20]. The calculations were done with the usual value of U and Hund's coupling J_H chosen for Ir with $U_{\rm eff} (\equiv U - J_H) = 1.5$ eV in the Dudarev scheme [21]. In order to achieve convergence of energy eigenvalues, the kinetic energy cutoff of the plane-wave basis was chosen to be 550 eV. The Brillouin-zone integrations were performed with an $8 \times 8 \times 8$ Monkhorst grid of k points. The symmetry-protected ionic relaxation of the experimentally obtained crystal structure was carried out within a VASP calculation using the conjugate-gradient algorithm until the Hellman-Feynman forces on each atom were less than the tolerance value of 0.01 eV/Å.

The t_{2g} crystal field splitting of our low-energy Hamiltonian were obtained retaining Ir t_{2g} within the basis set and downfolding higher degrees for freedom using the muffin-tin orbital (MTO) based Nth-order MTO (NMTO) method [22–24] as implemented in the STUTTGART code. The NMTO method relies on the self-consistent potentials borrowed from the linear MTO (LMTO) calculations [25]. For the self-consistent LMTO calculations within the atomic sphere approximation (ASA), the space filling in the ASA was obtained by inserting appropriate empty spheres in the interstitial regions.

III. RESULTS AND DISCUSSION

A. Structural and electronic characterizations

We start by probing the true dimensionality of SNIO, the degree of IrO_6 octahedral distortion, and the resultant noncubic crystal field, which will all be collectively manifested in the Ir-O bandwidth. Also, the extent of possible site disorder among Na and Ir is important because such a disorder can bring two Ir ions close to each other (Fig. S3 in the SM [3]), creating face-sharing Ir connectivity and strong Ir-O-Ir superexchange interactions. This may indeed influence the magnetic response of the system [26,27], especially if the bulk magnetic response truly becomes nonexistent ($J_{\rm eff} = 0$ for Ir^{5+} in the purely atomic strong SOC limit).

In order to confirm the Ir valence in this sample, the measured Ir L_3 XANES spectrum is shown in Fig. 2(a). The asymmetric structure of the spectral line, in the form of a weak shoulder on the lower-energy side [shown by the solid blue arrow in Fig. 2(a)], resembles quite well the Ir^{5+} oxidation state [28,29]. Further, the corresponding second derivative curve [inset in Fig. 2(a)] clearly indicates the presence of $2p \rightarrow t_{2g}$ (lower-energy feature) and $2p \rightarrow e_g$ (higher-energy peak) transitions. The peak shape and structure and the peak intensity corresponding to $2p \rightarrow t_{2g}$ transition affirm pentavalent Ir [28,29] in this compound.

In addition, the energy positions of the $4f_{7/2}$ and $4f_{5/2}$ features in the measured Ir $4f$ core level XPS spectrum [Fig. 2(b)] along with their spin-orbit separation of 3.1 eV support the pure 5+ charge state of Ir [30,31] in this material. The presence of pure Ir^{5+} species therefore serves as indirect proof to refute any kind of noticeable oxygen defect in the SNIO sample, as the change in oxygen stoichiometry would eventually affect the Ir oxidation state.

Detailed XRD as well as Ir L_3-edge EXAFS spectroscopy (Table S1, Figs. S1 and S2, and Table S2 in the SM [3]) indicate about 8%–10% Na/Ir antisite disorder (ASD) in the system. The results also reveal the distortion within the IrO_6 octahedra, which is summarized in Table S1 [also see Figs. 1(b) and 1(c)]. Such octahedral distortions are common in face-shared systems, which bring forth further splitting to the transition metal t_{2g} and e_g levels and modify the

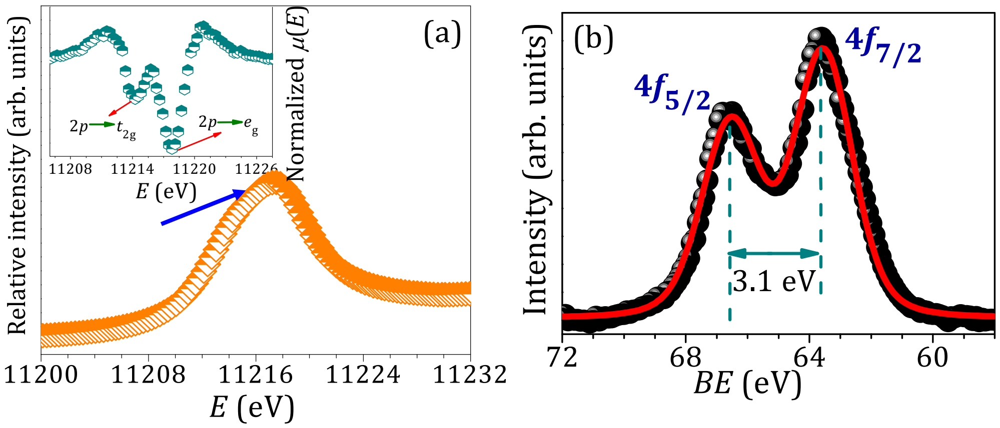

FIG. 2. (a) Ir L_3-edge XANES spectrum (half-filled orange triangles). Inset: respective second derivative curve (half-filled cyan hexagons). (b) Ir $4f$ core level XPS spectra (shaded black circles) along with the fitting (red solid line).

bandwidth. Therefore, next, we compare the low-resolution, high-energy Ir L_3-edge RIXS spectrum of SNIO [Fig. 1(e)] with that of BZIO [30], which possesses face-shared isolated $\mathrm{Ir_2O_9}$ dimers [Fig. 1(d)]. The very first observation is the presence of much broader bands in BZIO, which confirms that the effective spatial dimensionality is, indeed, substantially lower in SNIO. The pseudo-1D nature of SNIO in the *a-b* plane is shown in Fig. 1(b), while the enhanced Ir-Ir isolation along the *c* direction in SNIO compared to BZIO is more clearly presented in Figs. 1(c) and 1(d). The isolated nature of $\mathrm{Ir^{5+}}$ ions in SNIO and comparatively lower bandwidths offer the possibility to realize the nearly atomic SOC limit so that the $J_{\mathrm{eff}} = 0$ ground state may be realized. Moreover, like many other iridates, this compound is also found to be insulating by both XPS valence band and electrical resistivity measurements (Fig. S4 [3]), which indicates the clear prevalence of SOC in SNIO too.

In light of the above experimental observations, we first carry out non-spin-polarized DFT calculations which show a $t_{2g} - e_g$ splitting of ~3.5 eV within the Ir d states, consistent with the RIXS results [Fig. 1(e)]. The trigonal distortion of the $\mathrm{IrO_6}$ octahedra, furthermore, splits the t_{2g} states into low-lying a_{1g} and higher-lying doubly degenerate e_g^{π} states with a relatively small noncubic crystal field splitting of 0.05 eV. The nearly isolated Ir atoms in SNIO lead to a very narrow Ir t_{2g} bandwidth of 0.7 eV compared to those of other d^4 iridates, in which the bandwidth is typically 1.2–1.4 eV [30–33]. Inclusion of SOC within the GGA + SOC [17,18] formalism splits this narrow Ir t_{2g} state into completely filled single-particle $j_{\mathrm{eff}} = 3/2$ (Γ_8) and empty $j_{\mathrm{eff}} = 1/2$ (Γ_7) states, introducing an energy gap in the electronic structure [see Fig. 1(f)] and emphasizing the important role of SOC in causing the system to be insulating.

Next, the low-energy, high-resolution Ir L_3-edge RIXS spectra [34] from SNIO and BZIO are compared in Fig. 1(g). Clearly, there are substantial differences in the spectral width, intensity, and energy positions as well as the number of spectral features [peak at 0.18 eV in BZIO and the presence of weak asymmetry on the higher-energy side of the second and third peaks at ~0.34 and 0.6 eV, respectively, in SNIO, shown by bicolor arrows in Fig. 1(g)] between the two, which could be associated with an enhanced degree of hopping and greater extent of Ir t_{2g} trigonal crystal field splitting in BZIO [32] compared to SNIO. Moreover, there would be bimodal distributions of local noncubic crystal fields, Ir-O covalent interactions, Ir-Ir superexchange interactions $J_{SE}(\approx 4t^2/U)$, and the subsequent effective SOC strengths in SNIO due to the presence of ~90% Ir in the ordered sites along with ~10% Ir in the antisite positions, which is naturally absent in BZIO. However, as any attempt to directly estimate effective SOC λ_{eff} from the low-energy Ir L_3 RIXS data, assuming only atomic effects, is going to be futile [32,35], we refrain from making such an estimate here.

B. dc magnetic susceptibility and spin-polarized electronic structure calculations

Next comes the crucial question of whether the elusive $J_{\mathrm{eff}} = 0$ state is realized in SNIO or not. The bulk susceptibility χ vs temperature T study [Fig. 3(a)] and the consequent Curie-Weiss fit $[\chi(T) = \chi_0 + \frac{C}{T - \Theta_{CW}}]$ give the most direct answer to this question. It is important to stress here that the applicability of the Curie-Weiss fitting, including the choice of the temperature range of fitting and applied magnetic field, has been verified by the measured field-independent high-field dc susceptibility data in the chosen temperature region of fitting. However, contrary to the expectation, a high effective moment $\mu_{\mathrm{eff}} \approx 0.5\mu_B$/Ir with a Weiss temperature Θ_{CW} of -23.6 K was observed in SNIO. This observation directly refutes the single-ion description of iridium and endorses the previous results for isostructural compounds [5,7,8,10] depicting SNIO as a three-dimensional system. Moreover, the large value of the magnetic moment raises doubt about the high-SOC picture, and only an intermediate λ_{eff} in columnar systems [9,12] appears to be suitable. But it should also be noted that the existing Na/Ir site disorder may also affect the magnetic response to a significant level, as mentioned earlier. However, considering this site disorder to be the origin of finite magnetism in this system can be rejected from the observation of developed large local $\mathrm{Ir^{5+}}$ moments in the

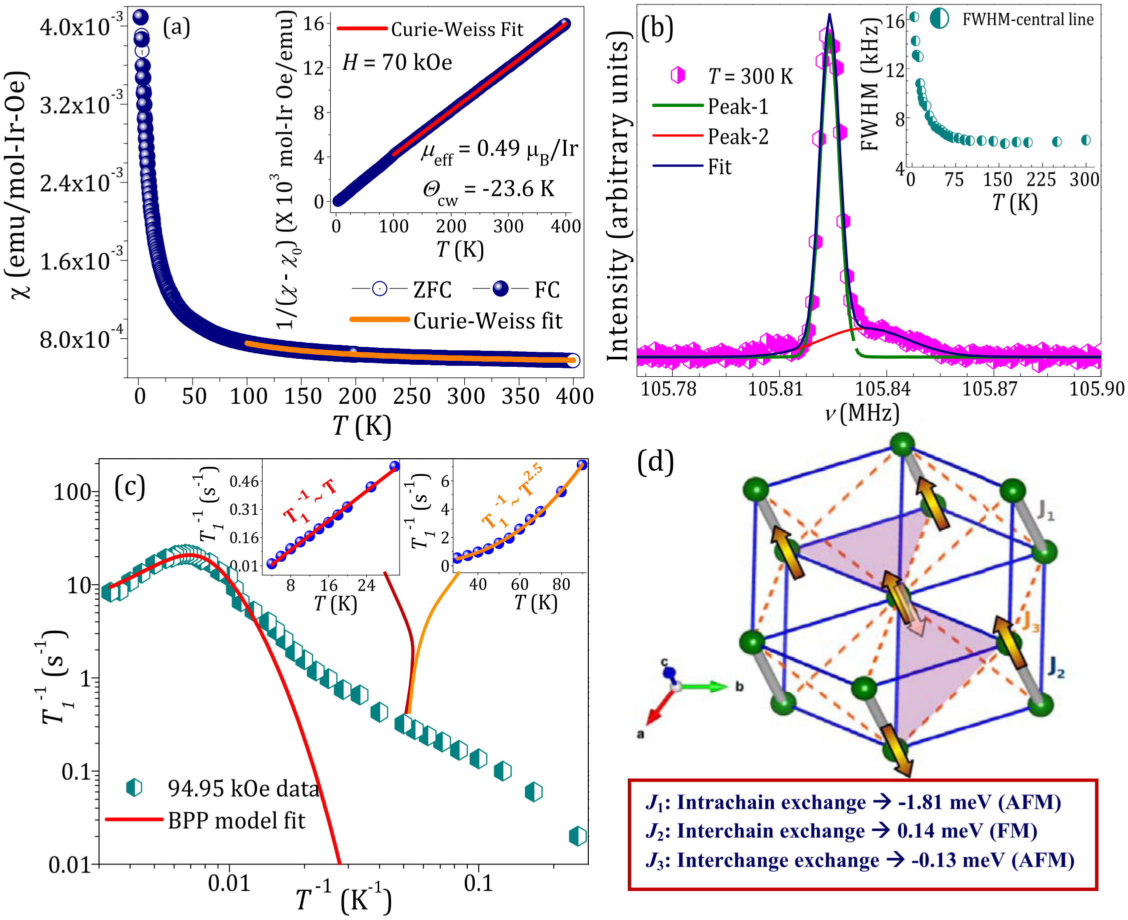

FIG. 3. (a) The 70 kOe dc susceptibility data along with Curie-Weiss fitting. (b) The 300 K ^{23}Na NMR spectrum along with the fit. Inset: T variation of the mainline width. (c) T evolution of the spin-lattice relaxation rate. Inset: power-law dependency below 90 K. (d) The edge-shared Ir triangular network (light violet region).

analogous Li counterpart, Sr_3LiIrO_6, with complete absence of Li-Ir antisite disorder [36]. Interestingly, spin-polarized GGA + SOC + U calculations with the spin quantization axis along the [001] direction (see Sec. II for details) not only show that an AFM configuration with antiparallel spin orientations in the neighboring Ir sites within each chain is slightly lower in energy ($\Delta E/\mathrm{f.u.} = 3$ meV) than the nonmagnetic structure but also computes large spin and orbital moments at the Ir site with values of $0.62\mu_B$ and $0.26\mu_B$, respectively, in contrast to the theoretical study of the nonmagnetic ground state by Ming *et al.* [37]. Moreover, in agreement with the observation of large local moments in SNIO, Kaushal *et al.* recently confirmed the generation of magnetic moments with existing short-range antiferromagnetic interactions among them in one-dimensional t_{2g}^4 iridate chains using the density matrix renormalization group (DMRG) technique [38].

C. ^{23}Na nuclear magnetic resonance

One important issue in such weakly magnetic materials could be the influence of extrinsic factors such as small paramagnetic impurities, which often lead to the low-temperature Curie-Weiss-like upturn on top of the intrinsic magnetic signal [39] of bulk magnetization. So we employed NMR as a complementary tool for probing intrinsic magnetism in this system. Consequently, ^{23}Na ($I = 3/2$) NMR was performed in a fixed field of 93.954 kOe and in the temperature range of 4–300 K, and the results are summarized in Figs. 3(b), 3(c) and S5. At room temperature, there is a clear knee on the high-frequency side [Fig. 3(b)] of the resonance line shape, where a fit with a combination of two Gaussians is found to be satisfactory. The relative intensity of the Gaussian centered on the knee is about 30%, while the main line constitutes about 70% of the spectral intensity. The peak positions and the relative intensities are found to be nearly temperature independent. There is a gradual broadening of the lines below 100 K, and consequently, at lower temperatures the knee becomes indistinguishable [40]. The presence of a second NMR signal ("knee" feature) is attributed to Na/Ir site disorder. At this point a quantitative understanding could be put forward in connecting the relative weight of the second resonance line with the Na/Ir ASD. In the ideal structure, the Na and Ir ions alternate to form a chain. Each Ir(Na) has two Na(Ir) neighbors. In the case of site disorder x (in percent) in the dilute limit, one will have a probability of finding a Na with no Ir neighbors of x^2, while that with only one Ir neighbor will be $2x(1-x)$, and the remaining fraction $(1-x)^2$ will be unaffected. In the dilute limit, then, a $2x$ intensity will appear in the second resonance, which is likely to be shifted due to a different chemical and magnetic environment. For higher x, other chemical environments become possible, and the mainline intensity gets depleted further. Given that a 10% ASD cannot be ruled out from our structural analysis, a 30% intensity appearing in the knee feature is consistent with Na/Ir site disorder. The variations of the ^{23}Na NMR shift and linewidth from the two-Gaussian fits between 30 and 300 K are shown in Figs. S5(a) and S5(b). The near absence of any variation in the NMR shift with temperature suggests weak hyperfine coupling of the ^{23}Na with magnetic Ir or that the moment on Ir is weak or perhaps both. But an increase in mainline width at low temperatures [see the inset in Fig. 3(b)] scales with the low-temperature $\chi(T)$ upturn [Fig. 3(a)], affirming the intrinsic nature of the observed large local Ir^{5+} moments in SNIO, as such an increase in linewidth arises from varying dipolar coupling interactions with the Ir^{5+} local moments. So the almost-temperature-independent NMR shift (Fig. S5(a) [3]) could certainly be attributed to the weak hyperfine coupling of ^{23}Na with Ir^{5+} moments considering the fact that the ^{23}Na nucleus tracks the local Ir moments via transferred hyperfine coupling through Ir(5d)-O(2p) orbital overlap. Furthermore, apart from confirming the intrinsic nature of Ir^{5+} moments in this sample, we performed linear fitting on the NMR mainline width versus 70 kOe dc magnetic susceptibility χ plot (Fig. S5(c) [3]), with temperature being an implicit parameter. The slope of the representative linear fit provides a dipolar coupling constant of about $A = 2.073 \times 10^{22}/\text{cm}^3$ atom. So it is reasonable to infer that this is due to dipolar interaction fields from the local Ir^{5+} moments, and the average distance between the local Ir^{5+} moments and the ^{23}Na nucleus is about 3.06 Å, further supporting the presence of intrinsic local Ir^{5+} moments in SNIO.

The ^{23}Na NMR spin-lattice relaxation rate $1/T_1$ was measured using a saturation recovery sequence. The recovery was found not to be single exponential. Considering that ^{23}Na has $I = 3/2$ and hence a quadrupole moment, one might expect a multiexponential recovery in the case when the full spectrum is not irradiated with the saturating sequence. However, given that the line shape is a combination of two species of Na, with both having a quadrupolar effect, we fitted the longitudinal nuclear magnetization recovery to a stretched exponential given by $M(t) = M_0\{1 - \exp[-(t/T_1)^\beta]\}$. The relaxation rate $1/T_1$ [shown in the main panel of Fig. 3(c)] increases with decreasing temperature and exhibits a broad maximum around 150 K. This maximum could not be associated with conventional spin glass freezing, where a critical slowing down of the spin fluctuations leads to a very short T_1 and hence a diverging spin-lattice relaxation at low and intermediate temperatures [41–43]. So we argue that this arises due to relaxation of the fluctuations arising from the motion of sodium ions. In the Bloembergen-Purcell-Pound (BPP) formalism [44,45], the relaxation rate varies as $\frac{\tau}{(1+\omega^2\tau^2)}$, where τ is the correlation time of the Na nuclear dipoles and ω is the NMR frequency. The correlation time (rate) follows Arrhenius behavior, $\tau = \tau_0 \exp(E_A/k_BT)$, where E_A is the activation energy. A maximum occurs around $\omega\tau = 1$. From the fit to our data [shown by the red solid line in the main panel of Fig. 3(c)], we obtain $E_A/k_B = 400$ K and $\tau_0 = 10^{-10}$ s. The ^{23}Na nuclear spin-lattice relaxation rate therefore appears to be dominated in this temperature region by the Na nuclear dipolar fluctuations and apparently remains unaffected by Ir local moment fluctuations. This might be due to the symmetric location of ^{23}Na between the magnetic Ir atoms where the antiferromagnetic fluctuations are filtered out. But below about 90 K, $1/T_1$ decreases upon further cooling and displays a power-law behavior [inset in Fig. 3(c)]. This suggests development of magnetic correlations among the Ir local moments in this low-temperature region, likely in agreement with the μSR relaxation rate below ~100 K [see Fig. 4(b)]. Such power-law dependence of $1/T_1$ could certainly be attributed to the existence of a gapless spin excitation spectrum in SNIO, which is consistent with other iridates ($\text{Na}_4\text{Ir}_3\text{O}_8$ [46] and $\text{Ba}_3\text{InIr}_2\text{O}_9$ [47]) and also other low-dimensional quantum materials [41,48,49].

D. Incompatible lattice topology and local spin-spin interactions

In order to understand the magnetic interactions between the large intrinsic Ir spins and for a quantitative estimation of the Ir-Ir exchange couplings, we have calculated the symmetric exchange interactions J^s by mapping the total energies, computed within GGA + SOC + U, of several spin configurations to the Heisenberg spin model $H_{\text{spin}} = \sum_{ij} J^s_{ij}(\vec{S}_i \cdot \vec{S}_j)$. Our calculations show that the dominant interaction J_1, corresponding to the nearest-neighbor (NN) intrachain Ir-Ir coupling, is AFM in nature with a magnitude of 1.8 meV. The second- and third-NN interactions, J_2 and J_3, corresponding to the interchain Ir-Ir interactions, are weaker and are, respectively, ferromagnetic (FM) and AFM in nature. Interestingly, both J_2 and J_3 have six NNs, and their magnitudes are also comparable, viz., $J_2 = 0.14$ meV and $J_3 = 0.13$ meV, resulting in a frustrated triangular network, as indicated in Fig. 3(d), prohibiting any long-range magnetic order from stabilizing in the system.

E. Muon spin rotation/relaxation study

To experimentally probe the real local internal magnetic fields and spin dynamics of this sample, we performed μSR experiments. The measured time evolution of the muon polarization $P(t)$ [50] in zero external field is shown in Fig. 4(a) for some selected temperatures from 40 mK to 300 K. Remarkably, upon cooling down, a fast initial relaxation develops, as can be seen by the loss of initial polarization. Meanwhile, the longer-time relaxation remains moderate and hardly changes throughout the whole temperature range. To monitor this evolution we fit the zero-field (ZF) polarization curves at all temperatures with the minimal model:

$$P(t) = A_1 \exp(-\lambda_1 t) + (1 - A_1) \exp(-\lambda_2 t), \tag{1}$$

where the first exponential component accounts for the fast front end with a relative weight A_1 and the second component stands for the slower relaxing tail. The relaxation rate λ_2 for the slow component is small and weakly T dependent, varying between 0.31(5) and 0.42(1) μs^{-1} [see Fig. 4(c)] in the whole temperature range. The temperature evolution of the fast relaxation rate λ_1 and its relative weight fraction are presented in Fig. 4(b). Below about 100 K, there is a sharp increase in λ_1, demonstrating the slowing down of the spin fluctuations, likely due to the enhancement of spin correlations for an increasing volume fraction A_1 of the sample. At still lower temperatures, the spin dynamics strikingly reaches a T-independent regime from about 30 K down to the lowest measurement at 0.04 K. Despite such obvious slowing down

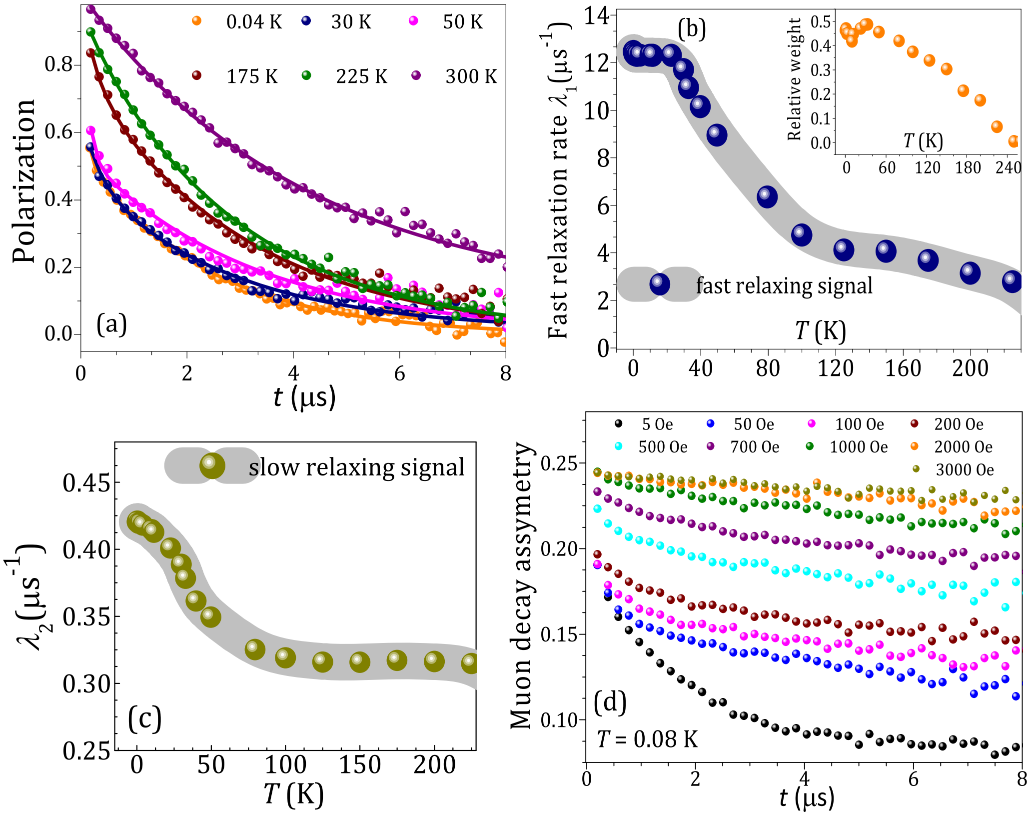

FIG. 4. (a) Time evolution of ZF muon polarization. (b) Temperature dependence of the fast relaxation rate. Inset: corresponding T variation in the relative weight fraction. (c) Temperature dependence of the slow relaxation rate. (d) Evolution of muon polarization at 0.08 K with applied external longitudinal fields.

of the spin dynamics, the system does not undergo any magnetic transition, and the spins continue to fluctuate far below the magnetic interaction energy scale $k_B\Theta_{CW}$. The absence of a "1/3 tail" and of spontaneous oscillations down to 40 mK confirms the dynamic nature of the local internal fields in the ground state of SNIO. Moreover, since the fraction A_1 evolves with T, the two components in the model do not stand for two muon sites. Rather, in the low-T regime, $A_1 \sim 0.5$ points at a strong inhomogeneity of the ground state.

In order to get further insight into the origin of the relaxation observed at low temperatures, we investigate the evolution of the muon polarization at $T = 0.08$ K under several external longitudinal fields, as shown in Fig. 4(d). Besides the fast decoupling for applied fields <20 G of a static component from nuclear fields, the recovery of the polarization appears to be very gradual, with sizable decoupling for low fields but relaxation persisting up to 3000 G, in line with a dynamical relaxation. The gradual decoupling could not be reproduced with a simple model with two dynamical components. This suggests again a broad distribution of internal fields and fluctuations in the ground state for which Eq. (1) is a rather simplistic approximation. Indeed, as a result of the ~8%-10% Na/Ir antisite disorder, there would be a distribution of local Ir^{5+} magnetic moments, which supports the strong inhomogeneous nature of a QSL ground state in this material.

At this point, what is quite surprising is the discrepancy between the nature of the NMR spin-lattice relaxation rate $\frac{1}{T_1}$ [inset in Fig. 3(c)] and that of the μSR relaxation rate λ_1^{-1} [Fig. 4(b)], possibly due to the difference in the respective characteristic time windows to which the NMR and μSR techniques are sensitive. While the temperature-independent λ_1^{-1} in the 30-0.04 K range [Fig. 4(b)] can be assigned to the signature of configurationally degenerate phases with fluctuating order [51], recent local density approximation calculations, on the other hand, show the possibility of local deformations around the environment of positive charge muons (i.e., the muon stopping sites), which would hence affect the local spin dynamics close to the muon probe [52].

F. Heat capacity investigation

The persisting spin fluctuations should also be reflected in the magnetic entropy. So to further explore the magnetic ground state, heat capacity was measured (C_p versus T) in zero and applied magnetic fields [Fig. 5(a)]. No sharp λ-like anomaly, the hallmark of a thermodynamic phase transition, was observed in the C_p data. However, below ~10 K, the presence of a weak humplike feature and its magnetic field dependence suggest a two-level Schottky anomaly, possibly arising from the uncompensated site-disordered Ir^{5+} magnetic centers [53–55].

The measured C_p is composed of three parts: (i) lattice (C_{lattice}), (ii) two-level Schottky anomaly (C_{sch}), and (iii) correlated magnetic (C_M) contributions. In the absence of any suitable nonmagnetic counterpart, C_{lattice} for $\mathrm{Sr_3NaIrO_6}$ was

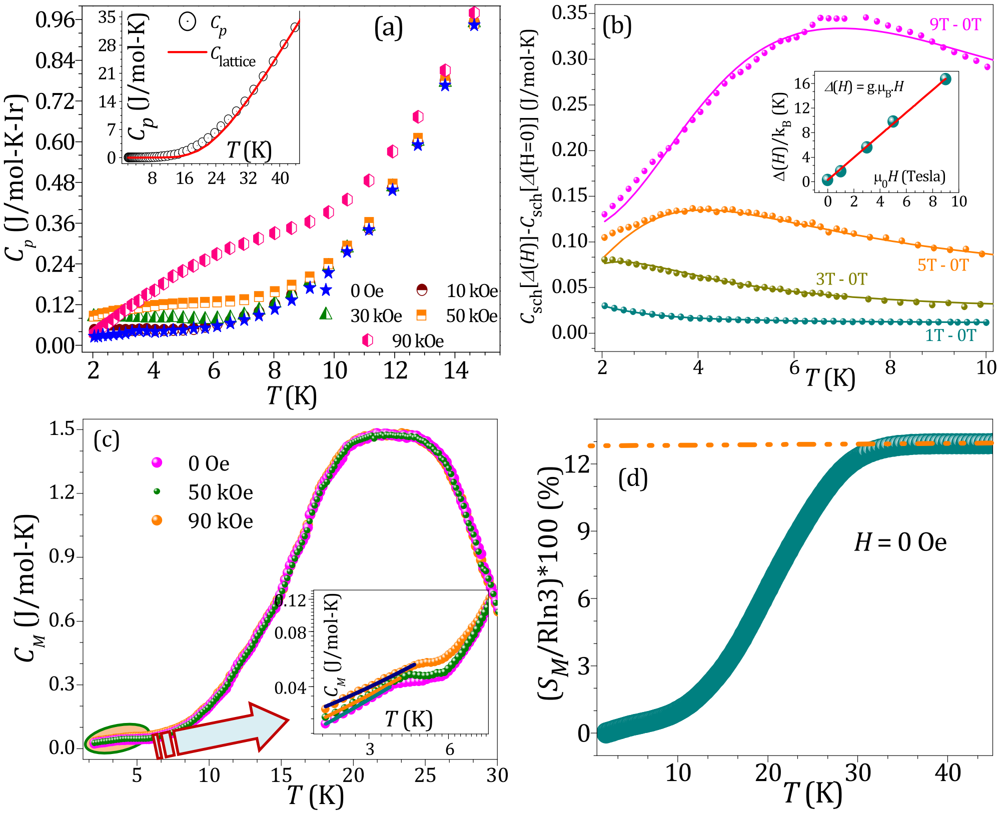

FIG. 5. (a) Temperature variations of the total specific heat C_p in the low-T region for zero field as well as different applied magnetic fields. Inset: lattice part extraction (solid red line) of the zero-field C_p data (open black circles). (b) Temperature variations of the $[C_p(H) - C_p(H = 0)]$ data at the respective applied magnetic fields along with the two-level Schottky anomaly fits (solid colored lines) in the low-T region. Inset: magnetic field dependence of the two-level Schottky energy gap (shaded dark cyan circles) and the linear fitting (solid dark red line). Temperature dependence of (c) magnetic specific heat and (d) magnetic entropy.

extracted after fitting the high-temperature zero-field C_p data (T range: 80–300 K) with the Debye-Einstein model, yielding a Debye temperature $\Theta_D = 409$ K. This high-temperature fitting was then extrapolated down to the lowest measured temperature of 2 K [inset in Fig. 5(a)] and taken as C_{lattice}, which was subtracted from the total C_p. The heat capacity of the sample is thus left out with ($C_M + C_{\mathrm{sch}}$). In order to obtain the correlated magnetic contribution C_M, the adopted strategy was to remove the Schottky part as follows: first, we subtracted the zero-field C_p data, i.e., $C_p(H = 0)$, from those measured in the applied magnetic fields, i.e., $C_p(H \neq 0)$. Consequently, the temperature variations of this difference ($\Delta C_{p,\mathrm{mag}}/T$) are illustrated in Fig. 5(b) and are modeled using

$$\frac{\Delta C_{p,\mathrm{mag}}}{T} = \frac{[C_p(H \neq 0, T) - C_p(H = 0, T)]}{T}. \quad (2)$$

This is then fitted with the two-level Schottky anomaly as

$$\frac{\Delta C_{p,\mathrm{mag}}}{T} = \frac{f}{T}[C_{\mathrm{sch}}(\Delta(H \neq 0)) - C_{\mathrm{sch}}(\Delta(H = 0))], \quad (3)$$

where f represents the percentage of isolated spin centers in the sample, $C_{\mathrm{sch}}(\Delta)$ and $C_{\mathrm{sch}}(\Delta_0)$ are the Schottky contributions to the specific heat, $\Delta(H)$ represents the Zeeman splitting in the applied magnetic field, and Δ_0 is the energy separation between the two levels at $H = 0$. $C_{\mathrm{sch}}(\Delta)$ is further defined as

$$C_{\mathrm{sch}}(\Delta) = R\left(\frac{\Delta}{k_BT}\right)^2 \frac{\exp(\Delta/k_BT)}{[1 + \exp(\Delta/k_BT)]^2}. \quad (4)$$

Correspondingly, the two-level Schottky anomaly fits are shown in Fig. 5(b). The fraction of isolated magnetic centers f is ∼5%-7%, which originates from the antisite-disordered Ir^{5+} magnetic centers, similar to the cases of some d^5 iridates [53,55]. The two-level Schottky splitting gap Δ/k_B follows a linear magnetic field dependence, $\Delta = g\mu_BH$ [inset in Fig. 5(b)], as expected for the free-spin Schottky anomalies [53–55]. The estimated g value found from this linear fit is about 2.5.

Finally, after subtracting the C_{lattice} and C_{sch} contributions, the T variations of the magnetic specific heat C_M are plotted in Fig. 5(c), clearly pointing towards a weak magnetic field dependence of C_M in the 2–8 K range. Such field dependency supports short-range magnetic correlations in the system. Further, C_M displays a broad maximum in the 20–25 K region, which remains unaltered under magnetic fields, indicating the highly frustrated nature of SNIO, as expected in spin liquids [41,56,57]. In addition, the linear temperature dependence of C_M along with the finite T-linear contribution [$C_M \approx \gamma T$, with γ being the Sommerfeld coefficient, and $\gamma \approx 10$ mJ/mol K^2, which remains nearly unchanged with the application of applied magnetic field, shown in the inset in Fig. 5(c)] is clearly evident. Such a finite T-linear contribution (i.e., nonzero Sommerfeld coefficient γ) to the low-temperature magnetic specific heat, which is unusual for a charge-gapped electrical insulator, arises due to gapless low-energy quasiparticle (spinon) excitations with a metal-like spinon Fermi surface, as discussed in the context of gapless quantum spin liquid candidates [31,41,56,58–64]. A similar gapless nature of spin excitations (the presence of metal-like spinon Fermi surface) in SNIO was further corroborated by the power-law dependency of the ^{23}Na NMR spin-lattice relaxation rate ($T_1^{-1} \sim T^n$) with a power of 2.5 in the T range of 30–90 K and a power of 1 in the T region below 30 K [inset in Fig. 3(c)], thus offering the exotic possibility of having gapless spin excitations from a spinon Fermi surface despite the energy-gapped charge sector, which can be considered a fingerprint of the gapless QSL material [41,47,48]. Finally, the release of magnetic entropy S_M [Fig. 5(d)] was found to be only ∼12.6% of the maximum $R \ln 3$ (≈9.134 J/mol K), affirming the persistent spin fluctuations and also low-energy spin excitations in this compound [61–64].

Overall, the magnetic entropy starts to decrease from around 30 K with decreasing temperature [Fig. 5(d)], which is exactly the temperature below which there is a complete absence of T evolution of the μSR relaxation [Fig. 4(b)], the magnetic field independent broad maximum appears in the C_M data [Fig. 5(c)], and the linear T-dependent NMR spin-lattice relaxation rate [inset in Fig. 3(c)] becomes evident. All these point towards the emergence of a rather unconventional inhomogeneous low-T (<30 K) spin liquid phase in SNIO.

G. Bandwidth vs moment comparison

Taking a clue from the observation of large Ir^{5+} moments in nearly 1D SNIO, we go on to plot the dependence of the calculated and experimentally observed magnetic moments as a function of theoretically predicted bandwidth from three columnar systems and BZIO in Fig. 6. We clearly see that the magnetic moment continues to decrease as the bandwidth gradually increases, which can be explained only if the spin-orbit coupling is weak, contrary to the general assumptions about iridates. In particular in a solid the strength of the SOC is renormalized as $\lambda_{\text{eff}} = \lambda_{\text{atomic}}/S$, where S is the total spin [65]. For d^4 systems with $S = 1$, SOC is much weaker than in d^5 systems with $S = 1/2$, providing further evidence that SOC for d^4 systems is always in the intermediate-coupling regime.

IV. CONCLUSION

Overall, our detailed experimental and theoretical results for the pseudo-1D columnar iridate Sr$_3$NaIrO$_6$ with the Ir^{5+} oxidation state reveal that this system fails to realize a $J_{\text{eff}} = 0$ state, resulting in a rather large local moment on Ir due to SOC in the intermediate-coupling regime, despite the significant isolation of Ir ions within the structure. Interestingly, the geometrical frustration also turns out to be extremely strong due to the comparable strengths of nearest- and next-nearest-neighbor exchange couplings, and as a result the system does not undergo any magnetic order down to at least 40 mK, even though the short-range spin-spin correlation starts to dominate from a temperature as high as 30 K, thus promoting a novel gapless quantum spin liquid ground state in SNIO.

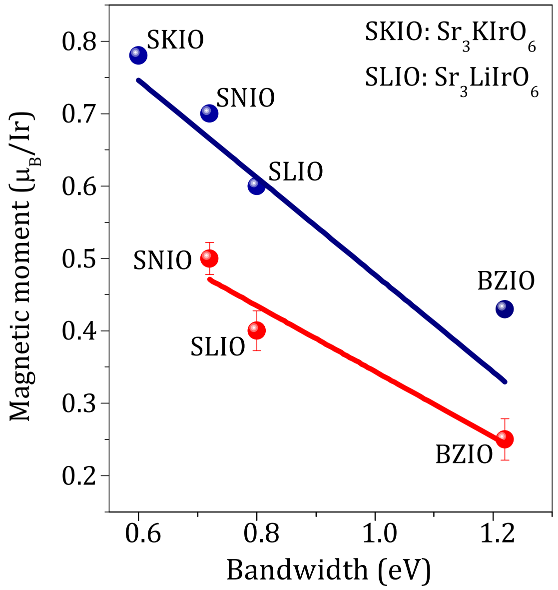

FIG. 6. Bandwidth dependence of effective Ir magnetic moments, obtained from experiments (red circles) and calculations (blue circles).

ACKNOWLEDGMENTS

A.B. thanks CSIR, India, and IACS for fellowships. A.B. also acknowledges SERB, DST, India, for a National Post Doctoral Fellowship (N-PDF, File No. PDF/2020/000785). S.B. thanks ETH Zurich for financial support. S.R. thanks the Technical Research Center of IACS, Indo-Italian POC, for support to carry out experiments in Elettra, Italy, and the Jawaharlal Nehru Centre for Advanced Scientific Research and SINP from the DST-Synchrotron-Neutron project for the support to perform experiments at ESRF (Proposal No. HC-2872) and ISIS-RAL, United Kingdom. S.R. also thanks SERB, DST, for funding (Project No. CRG/2019/003522). I.D. thanks the Science and Engineering Research Board (SERB), India (Project No. EMR/2016/005925), and the Department of Science and Technology-Technical Research Centre (DST-TRC) for financial support. T.S.D. acknowledges a J. C. Bose National Fellowship (Grant No. JCB/2020/000004) for funding.

---

[1] W. Witczak-Krempa, G. Chen, Y. B. Kim, and L. Balents, Annu. Rev. Condens. Matter Phys. **5**, 57 (2014).

[2] B. J. Kim, H. Jin, S. J. Moon, J. Y. Kim, B. G. Park, C. S. Leem, J. Yu, T. W. Noh, C. Kim, S. J. Oh, J. H. Park, V. Durairaj, G. Cao, and E. Rotenberg, Phys. Rev. Lett. **101**, 076402 (2008).

[3] See Supplemental Material at http://link.aps.org/supplemental/10.1103/PhysRevB.105.104431 for detailed structural investigations along with the structural parameters, electrical resistivity, valence band, and part of the NMR analysis.

[4] N. Segal, J. F. Vente, T. S. Bush, and P. D. Battle, J. Mater. Chem. **6**, 395 (1996).

[5] K.-S. Lee, H.-J. Koo, and M.-H. Whangbo, Inorg. Chem. **38**, 2199 (1999).

[6] S. Rayaprol and E. V. Sampathkumaran, Phys. Rev. B **71**, 094403 (2005).

[7] A. D. Hillier, D. T. Adroja, W. Kockelmann, L. C. Chapon, S. Rayaprol, P. Manuel, H. Michor, and E. V. Sampathkumaran, Phys. Rev. B **83**, 024414 (2011).

[8] D. G. Porter, M. S. Senn, D. D. Khalyavin, A. Cortese, N. Waterfield-Price, P. G. Radaelli, P. Manuel, H.-C. zur-Loye, C. Mazzoli, and A. Bombardi, Phys. Rev. B **94**, 134404 (2016).

[9] S. Calder, D. J. Singh, V. O. Garlea, M. D. Lumsden, Y. G. Shi, K. Yamaura, and A. D. Christianson, Phys. Rev. B **96**, 184426 (2017).

[10] P. A. McClarty, A. D. Hillier, D. T. Adroja, D. D. Khalyavin, S. Rayaprol, P. Manuel, W. Kockelmann, and E. V. Sampathkumaran, J. Phys. Soc. Jpn. **89**, 064703 (2020).

[11] D. Takegami *et al.*, Phys. Rev. B **102**, 045119 (2020).

[12] X. Liu, V. M. Katukuri, L. Hozoi, W.-G. Yin, M. P. M. Dean, M. H. Upton, J. Kim, D. Casa, A. Said, T. Gog, T. F. Qi, G. Cao, A. M. Tsvelik, J. van den Brink, and J. P. Hill, Phys. Rev. Lett. **109**, 157401 (2012).

[13] J. Rodriguez Carvajal, Phys. B (Amsterdam, Neth.) **192**, 55 (1993).

[14] M. Newville, J. Synchrotron Radiat. **8**, 322 (2001).

[15] B. Ravel, and M. Newville, J. Synchrotron Radiat. **12**, 537 (2005).

[16] J. P. Perdew, K. Burke, and M. Ernzerhof, Phys. Rev. Lett. **77**, 3865 (1996).

[17] G. Kresse and J. Hafner, Phys. Rev. B **47**, 558 (1993).

[18] G. Kresse and J. Furthmüller, Phys. Rev. B **54**, 11169 (1996).

[19] P. E. Blöchl, Phys. Rev. B **50**, 17953 (1994).

[20] G. Kresse and D. Joubert, Phys. Rev. B **59**, 1758 (1999).

[21] S. L. Dudarev, G. A. Botton, S. Y. Savrasov, C. J. Humphreys, and A. P. Sutton, Phys. Rev. B **57**, 1505 (1998).

[22] O. K. Andersen and T. Saha-Dasgupta, Phys. Rev. B **62**, R16219 (2000).

[23] O. K. Andersen, T. Saha-Dasgupta, R. W. Tank, C. Arcangeli, O. Jepsen, and G. Krier, Electronic structure and physical properties of solids, in *The Uses of the LMTO Method*, Lecture Notes in Physics (Springer, Berlin, 2000), Vol. 535, p. 3.

[24] O. K. Andersen, T. Saha-Dasgupta, and S. Ezhov, Bull. Mater. Sci. **26**, 19 (2003).

[25] O. K. Andersen and O. Jepsen, Phys. Rev. Lett. **53**, 2571 (1984).

[26] Q. Chen, C. Svoboda, Q. Zheng, B. C. Sales, D. G. Mandrus, H. D. Zhou, J.-S. Zhou, D. McComb, M. Randeria, N. Trivedi, and J.-Q. Yan, Phys. Rev. B **96**, 144423 (2017).

[27] M. A. Laguna-Marco, E. Arias-Egido, C. Piquer, V. Cuartero, L. Hernández-López, P. Kayser, J. A. Alonso, J. A. T. Barker, G. Fabbris, C. A. Escanhoela, Jr., and T. Irifune, Phys. Rev. B **101**, 014449 (2020).

[28] J.-H. Choy, J. D.-K. Kim, G. Demazeau, and D. Y. Jung, J. Phys. Chem. **98**, 6258 (1994).

[29] J.-H. Choy, J. D.-K. Kim, S.-H. Hwang, G. Demazeau, and D. Y. Jung, J. Am. Chem. Soc. **117**, 8557 (1995).

[30] A. Nag, S. Middey, S. Bhowal, S. K. Panda, R. Mathieu, J. C. Orain, F. Bert, P. Mendels, P. G. Freeman, M. Mansson, H. M. Ronnow, M. Telling, P. K. Biswas, D. Sheptyakov, S. D. Kaushik, V. Siruguri, C. Meneghini, D. D. Sarma, I. Dasgupta, and S. Ray, Phys. Rev. Lett. **116**, 097205 (2016).

[31] A. Nag, S. Bhowal, A. Chakraborty, M. M. Sala, A. Efimenko, F. Bert, P. K. Biswas, A. D. Hillier, M. Itoh, S. D. Kaushik, V. Siruguri, C. Meneghini, I. Dasgupta, and S. Ray, Phys. Rev. B **98**, 014431 (2018).

[32] A. Nag, S. Bhowal, M. M. Sala, A. Efimenko, I. Dasgupta, and S. Ray, Phys. Rev. Lett. **123**, 017201 (2019).

[33] A. Nag, S. Bhowal, F. Bert, A. D. Hillier, M. Itoh, I. Carlomagno, C. Meneghini, T. Sarkar, R. Mathieu, I. Dasgupta, and S. Ray, Phys. Rev. B **97**, 064408 (2018).

[34] M. Moretti Sala, K. Martel, C. Henriquet, A. Al Zein, L. Simonelli, C. Sahle, H. Gonzalez, M.-C. Lagier, C. Ponchut, S. Huotari, R. Verbeni, M. Krisch, and G. Monaco, J. Synchrotron Radiat. **25**, 580 (2018).

[35] A. Revelli, M. Moretti S. G. Monaco, P. Becker, L. Bohatý, M. Hermanns, T. C. Koethe, T. Fröhlich, P. Warzanowski, T. Lorenz, S. V. Streltsov, P. H. M. van Loosdrecht, D. I. Khomskii, J. van den Brink, and M. Grüninger, Sci. Adv. **5**, eaav4020 (2019).

[36] A. Bandyopadhyay, A. Chakraborty, S. Bhowal, V. Kumar, M. M. Sala, A. Efimenko, C. Meneghini, I. Dasgupta, T. Saha Dasgupta, A. V. Mahajan, and S. Ray, arXiv:2111.00925.

[37] X. Ming, X. Wan, C. Autieri, J. Wen, and X. Zheng, Phys. Rev. B **98**, 245123 (2018).

[38] N. Kaushal, J. Herbrych, G. Alvarez, and E. Dagotto, Phys. Rev. B **104**, 235135 (2021).

[39] F. Hammerath, R. Sarkar, S. Kamusella, C. Baines, H.-H. Klauss, T. Dey, A. Maljuk, S. Gaß, A. U. B. Wolter, H.-J. Grafe, S. Wurmehl, and B. Büchner, Phys. Rev. B **96**, 165108 (2017).

[40] In field sweep measurements of the spectra at lower frequencies/fields, we could observe a quadrupolar powder pattern with $\nu_Q \approx 0.1$ MHz in addition to the knee feature. In our fixed field measurements where the line shape is obtained with the Fourier transform of the echo, the satellites are out of the spectral width.

[41] P. Khuntia, S. Manni, F. R. Foronda, T. Lancaster, S. J. Blundell, P. Gegenwart, and M. Baenitz, Phys. Rev. B **96**, 094432 (2017).

[42] J. A. Quilliam, F. Bert, R. H. Colman, D. Boldrin, A. S. Wills, and P. Mendels, Phys. Rev. B **84**, 180401(R) (2011).

[43] Y. Shimizu, K. Miyagawa, K. Kanoda, M. Maesato, and G. Saito, Phys. Rev. Lett. **91**, 107001 (2003).

[44] N. Bloembergen, E. M. Purcell, and R. V. Pound, Nature (London) **160**, 475 (1947).

[45] N. Bloembergen, E. M. Purcell, and R. V. Pound, Phys. Rev. **73**, 679 (1948).

[46] A. C. Shockley, F. Bert, J.-C. Orain, Y. Okamoto, and P. Mendels, Phys. Rev. Lett. **115**, 047201 (2015).

[47] T. Dey, M. Majumder, J. C. Orain, A. Senyshyn, M. Prinz-Zwick, S. Bachus, Y. Tokiwa, F. Bert, P. Khuntia, N. Büttgen, A. A. Tsirlin, and P. Gegenwart, Phys. Rev. B **96**, 174411 (2017).

[48] J. Yoshitake, J. Nasu, and Y. Motome, Phys. Rev. Lett. **117**, 157203 (2016).

[49] P. Mendels and F. Bert, J. Phys. Soc. Jpn. **79**, 011001 (2010).

[50] To compare different measurements, we computed the polarization $P(t) = [A(t) - A_b]/[A(t=0) - A_b]$, where $A(t)$ is the measured asymmetry with $A(t=0) \sim 0.28$ and A_b is the asymmetry of the muon stopping in the sample holder, which was different in the dilution fridge and He flow setups.

[51] R. Dally, T. Hogan, A. Amato, H. Luetkens, C. Baines, J. Rodriguez-Rivera, M. J. Graf, and S. D. Wilson, Phys. Rev. Lett. **113**, 247601 (2014).

[52] F. R. Foronda, F. Lang, J. S. Möller, T. Lancaster, A. T. Boothroyd, F. L. Pratt, S. R. Giblin, D. Prabhakaran, and S. J. Blundell, Phys. Rev. Lett. **114**, 017602 (2015).

[53] T. Dey, A. V. Mahajan, P. Khuntia, M. Baenitz, B. Koteswararao, and F. C. Chou, Phys. Rev. B **86**, 140405(R) (2012).

[54] L. T. Corredor, G. Aslan-Cansever, M. Sturza, K. Manna, A. Maljuk, S. Gass, T. Dey, A. U. B. Wolter, O. Kataeva, A. Zimmermann, M. Geyer, C. G. F. Blum, S. Wurmehl, and B. Büchner, Phys. Rev. B **95**, 064418 (2017).

[55] R. Kumar, D. Sheptyakov, P. Khuntia, K. Rolfs, P. G. Freeman, H. M. Rønnow, T. Dey, M. Baenitz, and A. V. Mahajan, Phys. Rev. B **94**, 174410 (2016).

[56] L. Balents, Nature (London) **464**, 199 (2010).

[57] J. G. Cheng, G. Li, L. Balicas, J. S. Zhou, J. B. Goodenough, C. Xu, and H. D. Zhou, Phys. Rev. Lett. **107**, 197204 (2011).

[58] M. A. de Vries, A. C. Mclaughlin, and J. W. G. Bos, Phys. Rev. Lett. **104**, 177202 (2010).

[59] L. Clark, J. C. Orain, F. Bert, M. A. De Vries, F. H. Aidoudi, R. E. Morris, P. Lightfoot, J. S. Lord, M. T. F. Telling, P. Bonville, J. P. Attfield, P. Mendels, and A. Harrison, Phys. Rev. Lett. **110**, 207208 (2013).

[60] Y. Shen, Y.-D. Li, H. Wo, Y. Li, S. Shen, B. Pan, Q. Wang, H. C. Walker, P. Steffens, M. Boehm, Y. Hao, D. L. Quintero-Castro, L. W. Harriger, M. D. Frontzek, L. Hao, S. Meng, Q. Zhang, G. Chen, and J. Zhao, Nature (London) **540**, 559 (2016).

[61] Z. A. Kelly, M. J. Gallagher, and T. M. McQueen, Phys. Rev. X **6**, 041007 (2016).

[62] O. Mustonen, S. Vasala, E. Sadrollahi, K. P. Schmidt, C. Baines, H. C. Walker, I. Terasaki, F. J. Litterst, E. Baggio-Saitovitch, and M. Karppinen, Nat. Commun. **9**, 1085 (2018).

[63] K. Kitagawa, T. Takayama, Y. Matsumoto, A. Kato, R. Takano, Y. Kishimoto, S. Bette, R. Dinnebier, G. Jackeli, and H. Takagi, Nature (London) **554**, 341 (2018).

[64] L. T. Nguyen and R. J. Cava, Phys. Rev. Materials **3**, 014412 (2019).

[65] D. I. Khomskii, *Transition Metal Compounds* (Cambridge University Press, Cambridge, 2014).